Journal of Rare Earths 41 (2023) 1429–1436

Contents lists available at ScienceDirect

Journal of Rare Earths

journal homepage: http://www.journals.elsevier.com/journal-of-rare-earths

A novel strategy to extract lunar mare KREEP-rich metal resources using a silicon collector☆

Chen Li [a, b], Kuixian Wei [a, *], Yang Li [b, **], Wenhui Ma [a, c], Yun Lei [a], Han Yu [a], Jianzhong Liu [b]

[a] Faculty of Metallurgical and Energy Engineering, Kunming University of Science and Technology, Kunming 650093, China
[b] Center for Lunar and Planetary Sciences, Institute of Geochemistry, Chinese Academy of Sciences, Guiyang 550081, China
[c] National Engineering Laboratory for Vacuum Metallurgy, Kunming University of Science and Technology, Kunming 650093, China

ARTICLE INFO

Article history:
Received 28 March 2022
Received in revised form
23 June 2022
Accepted 1 July 2022
Available online 6 July 2022

Keywords:
Lunar rare earth elements
In situ resource Utilization
Lunar mare ilmenite
Si reduction

ABSTRACT

The lunar mare potassium (K)-, rare-earth elements (REEs)- and phosphorous (P)-rich (KREEP-rich) region is a unique late-stage product of magma crystallization, in which ilmenite and incompatible elements have high grades, thus forming a giant natural reservoir. The extraction and purification of the high-value metal resources in the KREEP-rich region not only meet the construction needs of the lunar base but also solve the problem of resource scarcity on Earth. In this study, photovoltaic elemental silicon (Si) was used as a collector to extract ilmenite resources, REEs, and nuclear energy elements from basalt in the lunar mare KREEP-rich region at 1873 K. Based on experimentation, the metals titanium (Ti) and iron (Fe) in the lunar mare ilmenite are found to be enriched and solidified in the form of Si-based alloys. The contents of valuable incompatible elements in the KREEP-rich area are also found to be enriched and contained in the incompatible trace elements (ITEs) phase of the alloy. Among them, REEs (e.g., cerium (Ce) and thulium (Tm)) and nuclear elements (e.g., thorium (Th) and uranium (U)) are found to account for 82.61 wt% of the ITEs phase. This process provides a simple and feasible scheme for the *in-situ* resource utilization (ISRU) of the lunar surface and is suitable for the extraction and enrichment of lunar metal resources.

1. Introduction

The moon is the only natural satellite of Earth and has an advantageous spatial position. The establishment of a lunar base will be conducive to the realization of various scientific research and the exploration of other planets via the Chang'e project.[1] The climax of space exploration set off in the middle and late 20th century deepened the understanding of the moon and resulted in the accumulation of a large amount of data.[2] As an atmosphere-free body, the strong reducing environment on the lunar surface and unique geological events have caused abundant resources to be exposed to the lunar mare area on the surface.[3–5] Among these resources, the content of ilmenite in the high-titanium (Ti) basalt in the lunar mare area exceeds 15 wt%, and the content of ilmenite in some areas exceeds the mining grade on Earth.[6] This portion of the ilmenite resource reserves is huge and is distributed on the outermost layer of the moon, which means that it can be mined without complicated equipment. In addition, the content of rare-earth elements (REEs) in the KREEP rocks in the Oceanus Procellarum area is relatively high. In the KREEP-rich area, it is estimated that approximately 2.2×10^{17} m^3 of the KREEP lithosphere is preserved, and the contents of elements such as phosphorus (P) are also higher than that of lunar soil. The nuclear elements uranium (U) and thorium (Th) are also concentrated in KREEP.[4,6] The main occurrence of these incompatible elements is in the form of phosphate, and they exist in the forms of monazite, merrillite, etc.[7,8] Although the distribution of these trace elements does not reach the lower grade limit for extractable rare earth minerals on Earth, the limited volume and uneven distribution of the Earth's rare earth resources are objective.[9,10] As an additional reservoir of

☆ **Foundation item:** Project supported by the Yunnan Outstanding Youth Science Foundation (202101AV070007), the Reserve Talents of Young and Middle-aged Academic and Technical Leaders in Yunnan Province (2018HB009), and Strategic Priority Research Program of the Chinese Academy of Sciences (XDB 41000000).
* Corresponding author.
** Corresponding author.
E-mail addresses: kxwei2008@hotmail.com (K. Wei), liyang@mail.gyig.ac.cn (Y. Li).

https://doi.org/10.1016/j.jre.2022.07.002
1002-0721/

Earth's resources, the Moon's resources will also be valuable for mining as transportation costs decline.

In consideration of the load limitations and expensive Earth-moon transportation costs, *in-situ* resource utilization (ISRU) technology can overcome the high costs of ground-to-moon transportation and the need for long-term survival; ISRU includes the *in situ* additive manufacturing of lunar soil,[8,11–16] the utilization of oxygen,[17–19] hydrogen,[20–22] and water resources,[6,23–26] and the *in situ* utilization and extraction of metal resources.[2,17,18,21,22,27–30] However, there have been hardly any targeted studies on the extraction and enrichment of rare earth resources from the lunar surface. On Earth, for the extraction of REEs and nuclear elements such as Th and U, the smelting process requires hydrometallurgical processes such as acid or lye, or the active metal calcium (Ca) and other metals are required to thermally reduce the fluoride of REEs.[31–36] Although ISRU requires the provision of reactors as close as possible, the vacuum on the lunar surface and the variations in the day and night temperatures are not conducive to widespread hydrometallurgy, and the total amount of volatile electrolytes is reduced due to constant losses. However, regardless of which method is used, the necessity of large-scale equipment, complicated processes, and a variety of additives is unavoidable. This has introduced obstacles to the ISRU of REEs present in lunar KREEP resources. Therefore, metallurgical processes on the lunar surface should be shortened to the greatest extent by reducing the chemical extraction process and adopting a short-cycle smelting method. For the extraction and enrichment of REEs, elemental silicon, which is widely used in solar power generation, may be a suitable reducing agent. Therefore, a silicon reduction process was used in this study to extract metal resources from the lunar mare KREEP-rich region.

2. Experimental

In this study, the lunar mare simulant (LMS) prepared by Exolith Lab was used as the lunar mare sample, and its elemental content, mineral composition, particle size distribution, etc., were in line with the existing sample data. As exhibited in Table 1, the chemical composition of the minerals is mainly ilmenite, pyroxene, olivine, glass, etc.

The REEs in the KREEP-rich lunar mare area exist primarily in the form of phosphate, and natural monazite samples were used as raw materials. As presented in Table 2, monazite contains various REEs oxides. To simulate the KREEP-rich area with a low phosphate content, the simulated lunar soil sample with a content of 4 wt% was fully mixed. The high-purity Si used as a metal collector had a low content of impurities, and the impurities were therefore ignored in the experiment. The normal LMS and KREEP simulants were respectively mixed with the collector at a 4:1 mass ratio (20 g simulant with 5 g Si).

As shown in Fig. 1, a box-type atmosphere furnace was used as the heating instrument. The raw materials were first dried and then thoroughly mixed according to the determined proportions and were then placed in a magnesium oxide (MgO) crucible. The sample was then placed in a box-type atmosphere furnace that was evacuated to 1×10^4 Pa, after which high-purity argon (Ar) gas (99.99 wt%) was introduced to ensure that the sample underwent a reduction reaction under a lower oxygen partial pressure. The temperature was increased from room temperature at the rate of 10 K/min. After reaching 1873 K, the temperature was maintained for 2 h, after which the furnace was cooled. The samples were then removed, cut, broken, and polished, and tests were performed.

Table 2
The EPMA (10 points) chemical composition of the monazite sample.

Oxide	*w* (wt%)	Oxide	*w* (wt%)	Oxide	*w* (wt%)
SiO_2	4.70	Y_2O_3	1.21	Pr_2O_3	3.45
FeO	0.16	F	0.45	Gd_2O_3	1.95
P_2O_5	22.80	Ce_2O_3	22.69	ThO_2	17.81
Dy_2O_3	0.18	La_2O_3	6.05	UO_2	0.41
Tm_2O_3	0.20	Nd_2O	14.74		
ZrO_2	0.03	Sm_2O_3	4.07	Total	100.89

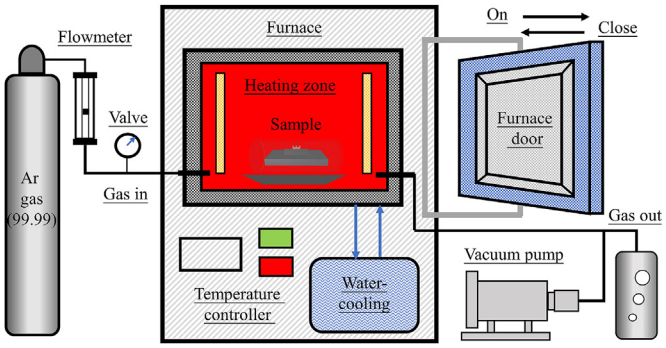

Fig. 1. The schematic diagram of the box atmosphere furnace.

Surface scanning via scanning electron microscopy (SEM) and energy-dispersive spectroscopy (EDS) was conducted to analyze the microscopic morphology and phase composition of the product (FEI Scios scanning electron microscope, America). The Maps 3.0 software included with the scanning electron microscope was used to model the entire reaction sample to eliminate the regional specificity of the analysis process. For the quantitative composition of each phase, electron probe microanalysis (EPMA) was conducted for composition measurement, and the corresponding mineral and metal standards were used for calibration (JEOL JXA-8530F Plus electron probe micro analysis, Japan). Micro-X-ray diffraction (micro-XRD) was used to measure the crystal structure of each phase to obtain accurate phase information (Rigaku Dmax Rapid V-type micro-X-ray diffraction, Japan). FactSage 8.0 thermodynamic calculation software was used to calculate the Gibbs free energy.[37,38] Furthermore, according to the actual reaction process, the phase diagram of the precipitated phase during the solidification process was drawn.

3. Results and discussion

3.1. Extraction of the main metal resources in lunar soil

Fig. 2 is the product profile of the LMS after the high-temperature liquid-phase reduction of Si. The two main phases in the product, which had distinct color differences, were the bright near-spherical metal and the dark lunar soil slag. The metal phase and the oxide phase exhibited good phase separation. Moreover,

Table 1
The XRF chemical composition of the simulated lunar soil sample.

Oxide	SiO_2	TiO_2	Al_2O_3	Cr_2O_3	FeO	MgO	MnO	CaO	Na_2O	K_2O	SO_3	Total
w (wt%)	42.81	4.62	14.13	0.21	7.87	18.89	0.15	5.94	4.92	0.57	0.11	99.56

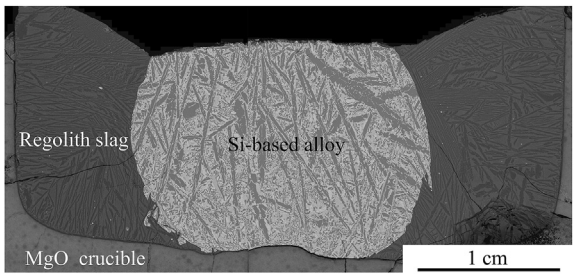

Fig. 2. The backscattered image of the Si reduction profile of the LMS.

the metal phase exhibited edge shrinkage in the form of a near-spherical shape, and the content of metal inclusions in the oxide was very low. This phenomenon demonstrates that the metal phase and the lunar soil melt had high interfacial tension at high temperatures, and thus had a good separation effect. Because the driving force of separation was not gravity sedimentation, the phase separation dominated by interfacial tension still exhibited better results even under lower gravity. Moreover, the interface of the MgO crucible was uneven and corroded, which indicates that a portion of the crucible material was dissolved in the slag.

EDS analysis was carried out at the slag-metallographic interface. As shown in Fig. 3, the two macroscopic slag and alloy phases can be identified by the presence or absence of oxygen (O). Among them, light metal elements such as Mg, Al, and Ca were found to be completely distributed in the slag phase, and metal elements such as Fe and Ti were completely distributed in the alloy phases, indicating that Si reduced the Fe and Ti contents in the LMS, which then transferred to the alloy phases, and extraction was realized. It can be seen from the distribution of cations that the molten slag was mainly divided into two phases, namely Mg-enriched areas and Al-, Ca-, etc., enriched areas.

In combination with the micro-XRD analysis of the product (Fig. 4(a, b)), it can be inferred that the Mg-enriched area was a forsterite (Mg_2SiO_4) phase, and the remaining part of the slag was an Al–Ca-enriched glass phase. In the alloy, the three main phases were a pure Si phase, a Si–Fe phase, and a Si–Fe–Ti phase. In comparison to the XRD analysis (Fig. 4(c, d)) and by searching for intermetallic compounds, it was found that the Si–Fe phase was Fe_2Si_5, and the Si–Fe–Ti phase was Si_2FeTi (τ_1). In the alloy phase, different metal elements exhibited distinct enrichment phases and formed intermetallic compounds, which demonstrates that different metals can be simply separated after cooling and crushing.

The phases of the crystalline precipitates of metals and oxides are displayed in the phase diagram. Fig. 5(a) presents the magnification of the end of Si-rich region of the Si–Fe–Ti ternary phase diagram, from which it can be seen that during the thermal reduction of Si, with the continuous replacement of Si in the alloy with Fe and Ti, the composition point of the metal phase gradually changed from the end-member point of pure Si to the Fe and Ti ends. Because the Fe and Ti contents in the simulated sample were limited by the composition of ilmenite ($FeTiO_3$ (1/1)) and other iron-containing minerals, such as pyroxene ($(Ca, Mg, Fe)_2SiO_6$) and olivine ($(Fe, Mg)_2SiO_4$), and the Fe/Ti atomic ratio was always greater than 1. The "I" and "II" areas in the phase diagram respectively represent the precipitation order of the Si–Fe and Si–Fe–Ti phases in the alloy system. In the "I" region, the τ_1 phase had priority over the precipitation of Si–Fe phase, and in the "II" region, the Si–Fe phase was precipitated first, after which the τ_1 phase was precipitated. The red line in the middle represents the boundary line of the composition point of the eutectic, i.e., the point at which

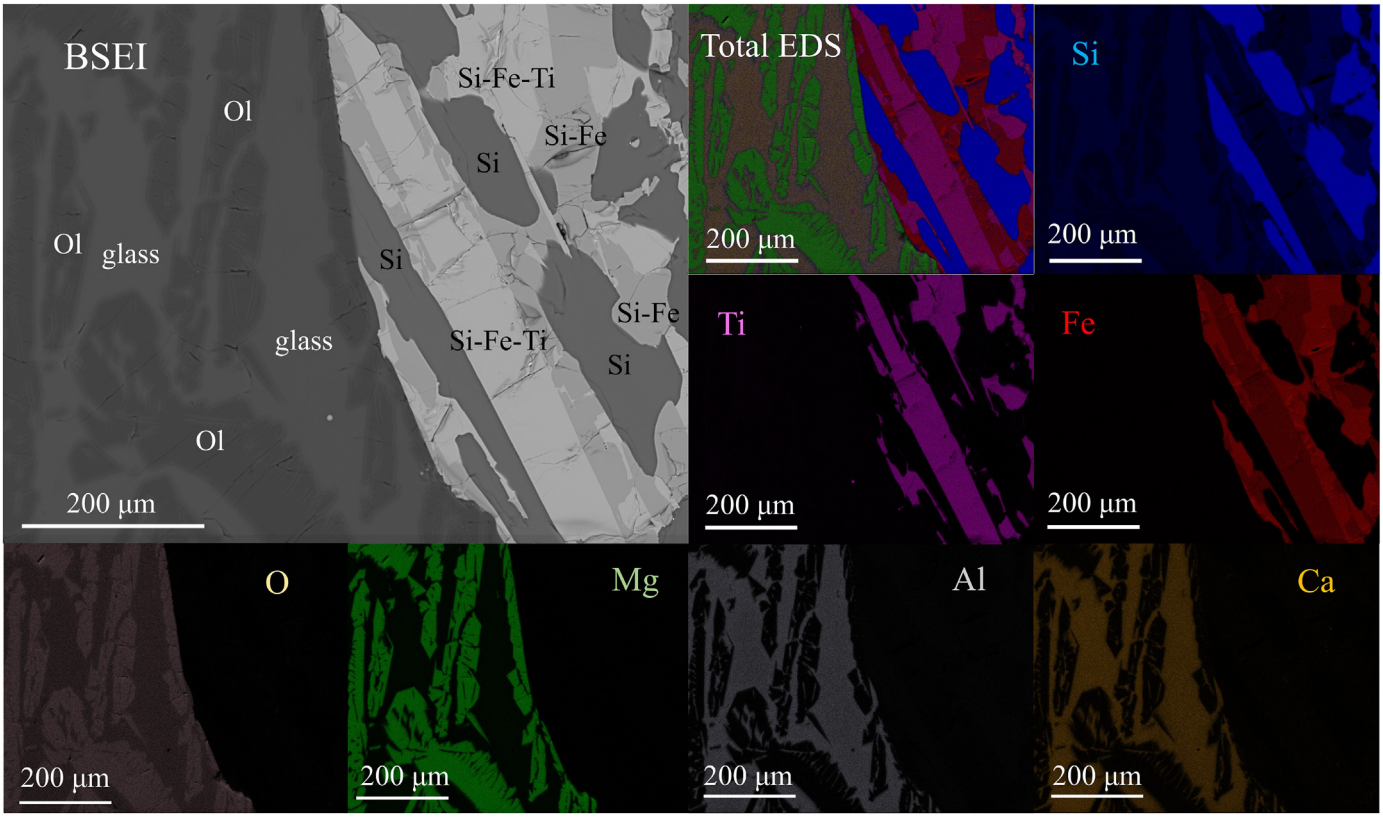

Fig. 3. The EDS mappings of the Si-reduced slag-metallographic interface of the LMS.

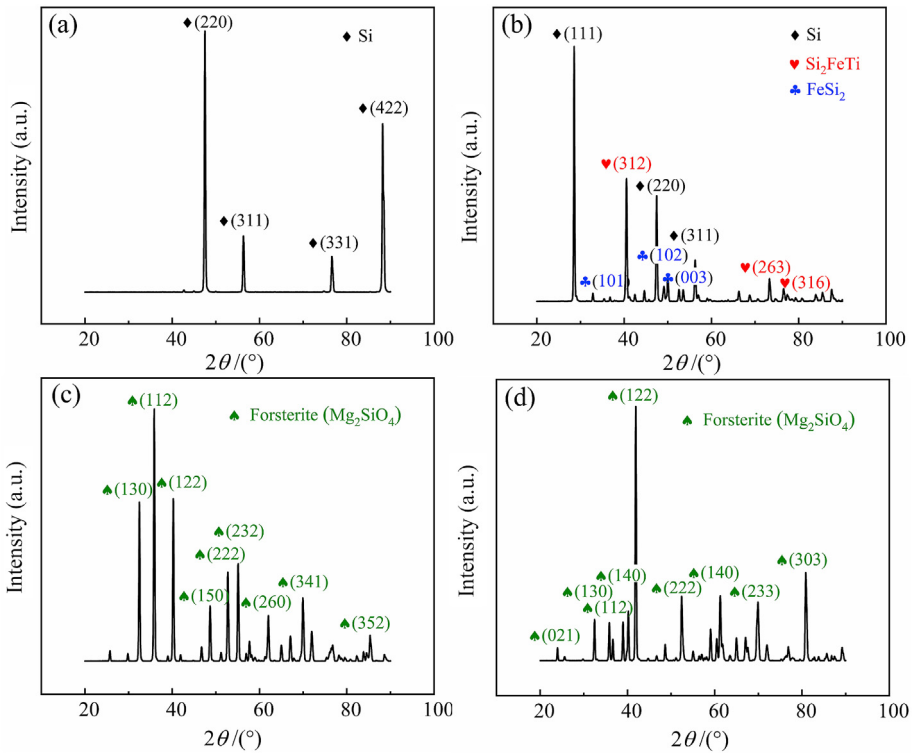

Fig. 4. The micro-XRD patterns of various phases in slag and alloy: (a) Forsterite; (b) Forsterite + glass; (c) Elemental Si; (d) Fe_2Si_5 (Si + $FeSi_2$) + Si_2FeTi.

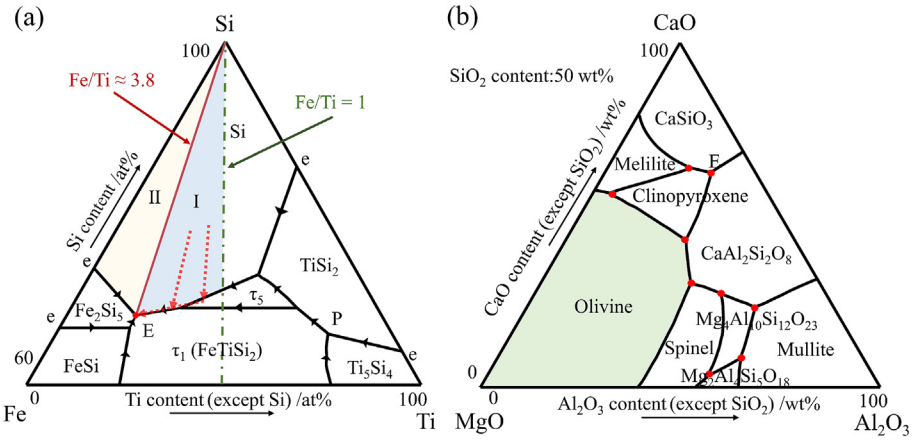

Fig. 5. The ternary phase diagrams of the reduction system. (a) Si–Fe–Ti alloy; (b) Final LMS slag.

the atomic ratio of Fe to Ti was approximately equal to 3.8. Because the atomic ratio of Fe to Ti in the actual sample was in the "I" (blue) region and no residual τ_5 alloy phase was found, it was determined that during the cooling process of the metal phase, along the red dotted line, pure Si was first precipitated, the τ_1 phase was then precipitated when the liquid phase reached the boundary, and, finally, the Fe_2Si_5 phase was precipitated.

The oxide slag was mainly composed of a forsterite phase with Mg_2SiO_4 as the main component, and a glass matrix was composed of light metals (Mg, Al, Ca, Na, etc.). The main components of the system after the reaction are represented by the phase diagram exhibited in Fig. 5(b). Both Fe and Ti were enriched in the metal phase, and the displacement reaction increased the SiO_2 content in the system. Because the crucible made of MgO was used as the container, the slag system partially dissolved the MgO, thereby causing the composition point of the slag enriched in MgO to be closer to that of MgO. As shown in the phase diagram, the first precipitated phases in the larger composition range near the MgO were all olivine, which confirms the rationality of the existence of needle-shaped olivine phases in the molten slag. Due to the limitations of the cooling time and rate, the viscosity of oxide slag increased sharply, which caused the mass transfer to be too difficult. Furthermore, a lower temperature and shorter cooling time were not sufficient to completely crystallize the matrix. The remaining MgO and the rest of the slag components formed a glass matrix.

3.2. Extraction of incompatible elements in the lunar KREEP-rich simulant

The Si-reduction result of the KREEP-rich simulant was roughly the same as the main process of the LMS, but REEs contained in it were reduced to the alloy phase by Si. However, a new phase appeared in the alloy, namely the high-concentration enrichment of the incompatible trace elements (ITEs) of REEs, including P, Th, and U, as shown in Fig. 6.

Via the backscattered electron analysis of the phase distribution and composition of the alloy product, it was found that there were four metal phases in the alloy, and they had large compositional differences. The matrix was elemental Si, and the metal phase with a relatively uniform distribution and a larger area was the Si–Fe phase; moreover, the Si–Fe–Ti phase was mostly distributed in the Si–Fe phase, and the two phases were adjacent to and interlaced with each other. In contrast, the brightest alloy phase was the rare-earth metal-ITEs phase, which was composed of REEs (Ce, Pm and Nd), P, Zr, Th, U and other elements. REEs were reduced to metallic elements in the alloy. During the solidification process, due to their large radius, REEs could not be dissolved in other alloy phases; they could only be discharged by the first solidified phase and sandwiched between the grain boundaries of other alloy phases. In this way, these rare metal elements were enriched to form a higher-purity alloy phase. From the EDS surface scanning results, it was found that in the ITE-rich phase, the contents of elements such as Si, Fe and Ti were very low, and while there was a little amount of F, whose content was less than that of the Si–Fe phase. ITEs such as Ce, Nd, Sm, Th, U and P were almost completely distributed in the enriched phase. It can be seen that REEs were reduced to the metal phase by high-temperature heat, and they became concentrated in the ITEs phase after cooling, which facilitated the separation and purification of REEs and also ensured the purity of the Si matrix.

The existing position of the ITEs alloy was at the boundary of the Si–Fe phase, and its positional relationship is indicative of the precipitation order of the ITEs. This means that ITEs will enter the Si–Fe(Ti) metal phase after the precipitation of the main Si phase.

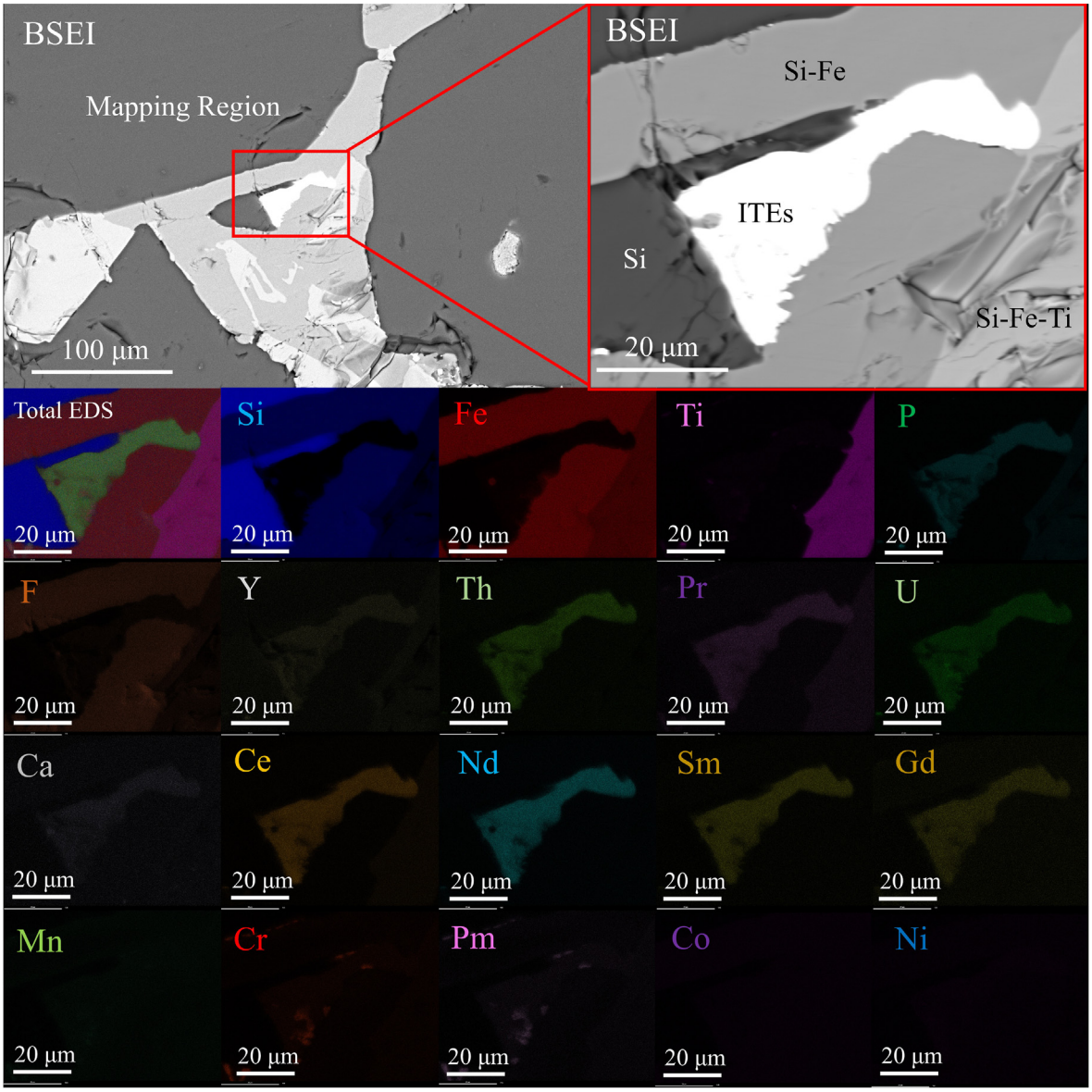

Fig. 6. The EDS mappings and element qualitative distribution maps of the Si-reduced alloy phase area in the KREEP-rich simulant.

Because the precipitation orders of the Si–Fe and Si–Fe–Ti phases were close, crystallization may be possible when the equipment is cooled down due to a large degree of undercooling. At this time, the ITEs will be precipitated from the Si–Fe phase. Because the Si content in the Si–Fe phase will be close to saturation, there will be no excessive Si element to form an alloy with the ITEs after solidification, so it will be precipitated in the form of a non-Si-based alloy. This precipitation form will eliminate the process of separation from the Si-based intermetallic compound product. In addition to the positional relationship between the metal phases, the distribution characteristics of the F element in the Si–Fe phase also support this inference.

The components of each phase in the alloy, including the ITEs and the main phases of the KREEP slag, are presented in Table 3, which reports the composition data obtained from the quantitative analysis of each phase by EPMA. It can be seen that in the ITEs phase, the total mass ratio of REEs to Th, U and other scattered elements reached 82.61 wt%. Among them, the light REEs i.e. La, Ce, Sm, Nd, Pr and other relatively high-content REEs accounted for a large proportion, and the contents of the medium and heavy REEs i.e. Gd (1.56 wt%) and Tm (0.31 wt%) in the minerals were extremely low. Furthermore, the hard-to-extract nuclear elements Th and U were also found to be enriched in the ITEs phase, which indicates that Si can extract and concentrate REEs and radioactive elements in the same phase at high temperatures. In the KREEP slag, the contents of Fe and Ti were extremely low. Compared with the initial composition, this may indicate that the metals entered the Si alloy. The olivine phase was pure forsterite, and the content of REEs in the glass phase was also below the detection limit. Based on these findings, it can be concluded that Si had a stronger effect on the extraction and enrichment of scattered elements. Unfortunately, although the ITEs were enriched in a variety of REEs, there were also very small amounts of dissolved REEs in other alloy phases. The presence of this portion of the dissolved REEs made it difficult to calculate the yield, because these REEs cannot separate phases independently, they would be difficult to be separated directly by mechanical crushing. As a result, the cost part cannot be simply and directly applied, and the dispersion and loss of REEs caused by this phenomenon are unavoidable in this process.

Table 3
The quantitative composition (wt%) of each phase of the REE alloy and KREEP slag determined by EPMA (10 points were selected and "bd" means below the exact detection limit 0.1%).

Elements	KREEP-alloy phases				Oxides	KREEP-slag phases	
	ITEs	Si	Si–Fe	Si–Fe–Ti		Olivine	Glass
Si	0.57	100.18	52.28	29.59	SiO_2	42.45	56.70
Ti	bd	bd	bd	30.21	TiO_2	bd	bd
Al	bd	bd	bd	bd	Al_2O_3	0.07	18.11
Fe	0.97	bd	43.19	33.66	FeO	bd	bd
Mg	bd	bd	bd	bd	MgO	56.76	7.72
Ca	0.61	bd	bd	bd	CaO	0.15	10.36
Na	bd	bd	bd	bd	Na_2O	bd	2.20
K	bd	bd	bd	bd	K_2O	bd	0.70
Mn	bd	bd	0.55	0.48	MnO	bd	bd
Cr	bd	bd	0.39	0.56	Cr_2O_3	bd	bd
Co	bd	bd	bd	bd	Co_2O_3	bd	bd
Ni	bd	bd	0.31	0.09	Ni_2O_3	bd	bd
P	14.45	bd	bd	3.39	P_2O_5	bd	bd
Dy	bd	bd	bd	bd	Dy_2O_3	bd	bd
Tm	0.31	bd	bd	bd	Tm_2O_3	bd	bd
Zr	0.17	bd	bd	bd	ZrO_2	bd	bd
Y	0.16	bd	bd	bd	Y_2O_3	bd	bd
F	0.54	bd	0.32	0.12	F	bd	bd
Ce	27.58	bd	bd	bd	Ce_2O_3	bd	bd
La	3.45	bd	bd	bd	La_2O_3	bd	bd
Nd	20.96	bd	bd	bd	Nd_2O_3	bd	bd
Sm	5.28	bd	bd	bd	Sm_2O_3	bd	bd
Pr	4.87	bd	bd	bd	Pr_2O_3	bd	bd
Gd	1.56	bd	bd	bd	Gd_2O_3	bd	bd
Th	16.76	bd	bd	bd	ThO_2	bd	bd
U	0.97	bd	bd	bd	UO_2	bd	bd
Total	99.29	100.20	97.25	98.26	Total	99.58	97.21

The general reaction process between the KREEP simulant and Si can be explained by the mechanism illustrated in Fig. 7. It is assumed that there is a reaction layer at the phase interface of the two incompatible liquid phases of the alloy melts and the slag. The reducing medium Si in the alloy melt replaces the transition metals Fe and Ti, and the ITEs P, REEs, Th, U, etc., in the melt. After the reaction, Si generates SiO_2 and enters the slag phase, while Fe, Ti, REEs, etc., enter the metal phase and dissolve. In particular, the decrease of the TiO_2 content in the melt increases the slag-alloy interfacial tension, which further promotes the phase separation of the alloy and slag. Although the extraction mechanism of the ITEs is the same as that of the transition metal elements, the enrichment (alloying) process cannot be specifically analyzed via phase diagrams due to unreferenced research.

FactSage 8.0 software was used to perform the thermodynamic estimation of the components present in the system, and the results are exhibited in Fig. 8. By reading the standard Gibbs free energy of the combination of metal elements and 1 mol O_2, the strength of the binding capacity between metals and oxygen was determined.[39] As a metal collector, Si has only enough reducibility to completely reduce the oxides of Fe, Cr, P, etc., into elemental substances.

The reducibility of Si can make Ti reduce to between 2–3 valences. In the same way, the ability of REEs, Th, U and other scattered elements to bind oxygen is also very strong. Therefore, if the metal thermal reduction process is used as the reaction pathway, the reduction of many metals from Ti is thermodynamically infeasible. At the high temperature of 1873 K, the deviation of the reactants and products from the standard state will greatly affect the free energy of the reaction, which follows the thermodynamic laws expressed by Eqs. (1) and (2):

$$\Delta G^{\Theta}_{\text{reaction}} = -RT \ln K_{1\ \text{mol}\ O_2} \tag{1}$$

$$\Delta G_{\text{real}} = \Delta G^{\Theta}_{\text{reaction}} + RT \ln \prod a^{\nu_B}_{B(1\ \text{mol}\ O_2)} \tag{2}$$

where $\Delta G^{\Theta}_{\text{reaction}}$ and ΔG_{real} respectively represent the Gibbs free energy change of the standard and actual reaction process, $K_{1\ \text{mol}\ O2}$ is the equilibrium constant when one mole of O_2 participates in the reaction, and $a^{\nu B}_{B(1\ \text{mol}\ O2)}$ is the activity of each component when one mole of O_2 participates in the reaction. It can be seen from the equations that in addition to the standard Gibbs free energy of each substance being able to affect the free

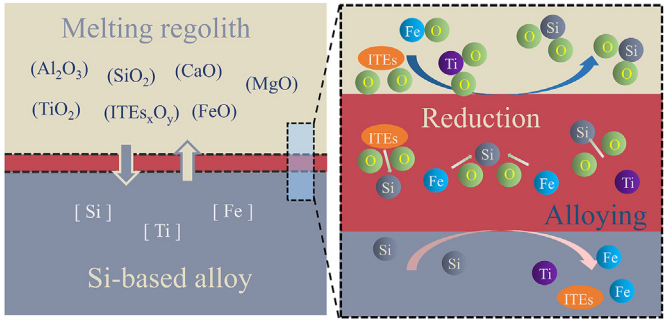

Fig. 7. The schematic diagram of the principle of Si thermal reduction.

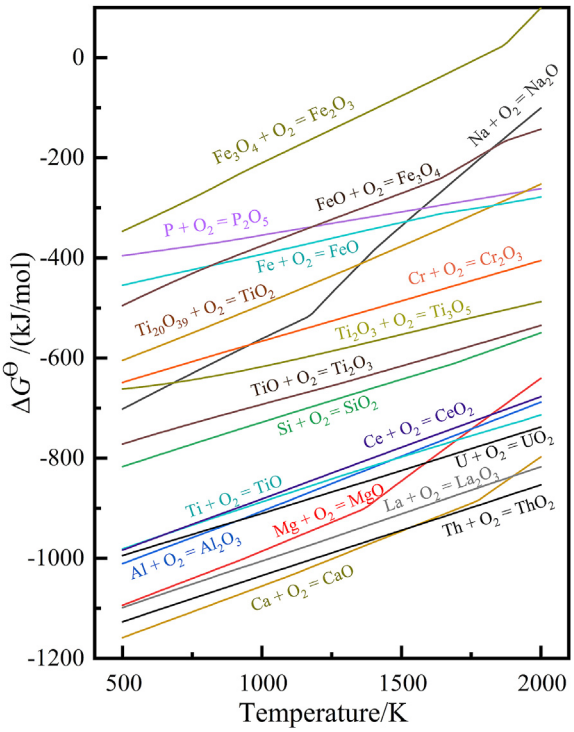

Fig. 8. The Ellingham diagram of the elements in the KREEP-rich area.

energy of the reaction, at higher temperatures, the state and activity of the reactants and products will also affect the progress of the reaction to a greater extent. In addition to the influence of standard state changes, such as activity, the formation of intermetallic compounds will also improve the stability of the product. In the oxide solution, Ti exists in the form of TiO_2, but in the cooled alloy, it forms the Si_2FeTi phase with Si and Fe; this intermetallic compound includes the mixed phases of Si_2Ti and Si_2Fe. Due to the formation of intermetallic compounds, the product is thermodynamically more stable, so the reaction can proceed across the oxygen potential. For nuclear elements such as Th and U, an alloy phase with only rare metals is formed in the metal phase, and a relatively uniformly distributed metal phase is formed between the Si substrate and the grain boundary of the Si–Fe alloy.

3.3. Technological application on the lunar surface

As shown in Fig. 9, the construction of the substrate requires continuous solar panels to provide power, and *in situ* extraction of Si resources and the application of photovoltaics require the purification of crude Si to solar-grade (or close to solar-grade) Si. Lunar soil is a ubiquitous oxide that can be used as a natural slagging agent for *in situ* slag refining and can help crude Si remove Al, Ca, B and other impurities.[40–42] Furthermore, via the thermal reduction properties of elemental Si, it can extract Fe and Ti from lunar ilmenite and can prepare Si–Fe and Si–Fe–Ti alloys during refining. Fe and Ti can then be separated to achieve *in situ* resource extraction. For KREEP rock, which is rich in rare metal elements, in addition to the purification of Fe and Ti, rare metals such as REEs, Th, U and other elements can also be obtained, and the ITEs phase can be enriched. After crushing, vacuuming, and other enrichment operations, the separation of incompatible elements, such as REEs, can be achieved, and these elements can then be used as a supplement to Earth's resources. The reducing environment of the lunar surface and the ability of the lunar soil to insulate radiation will allow for the safe storage of more active rare earth metals and radioactive elements at a low cost. With the continuous reduction of ground-to-moon transportation costs, the scarce resources extracted *in situ* can be stored or transported step by step under cost constraints.

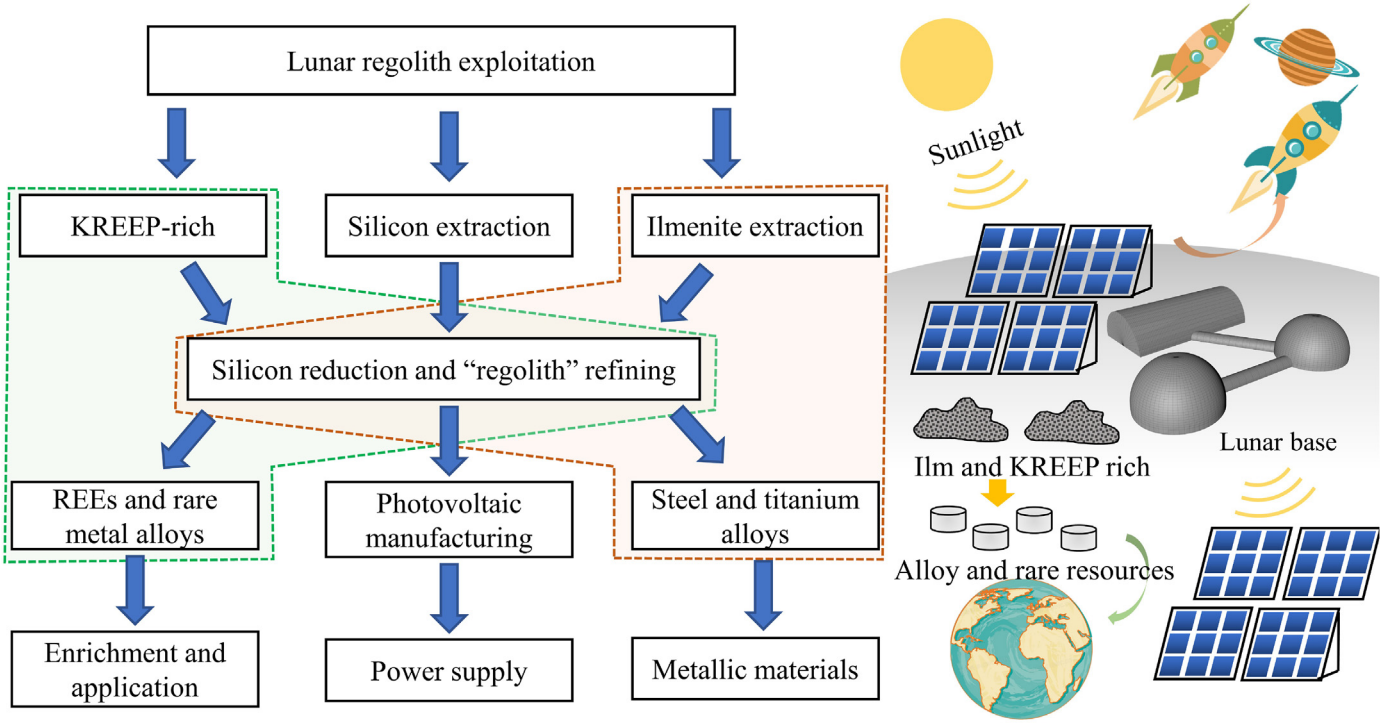

Fig. 9. The Si thermal reduction process and application assumptions.

However, the solubility of incompatible elements in Si alloys determines the lowest grade of this method for the extraction of rare earth metals; this content of the present study requires corresponding basic research as a theoretical basis. Moreover, the high-temperature thermodynamic data of REEs are not yet highly self-consistent, and there are no accurate thermodynamic data supporting for a variety of complex alloy systems.

4. Conclusions

This research proposes a simple and novel process for the extraction of metal resources from the KREEP-rich lunar mare area. Elemental Si, which can be used as a raw material for solar cells, is used as a metal collector. In this study, via the Si thermal reduction reaction principle, the metals Fe and Ti, REEs, and nuclear elements such as Th and U that have application value in the LMS and KREEP simulant were extracted. Moreover, by using the solidification law of the elements in the alloying process, the alloy phases rich in Fe, Ti, etc., as well as the ITEs phases were also extracted. Combined with various detection methods, it is demonstrated that elemental Si can extract and enrich the transition metals Fe and Ti, as well as REEs such as Ce, Nd, and other light REEs, and medium and heavy REEs including Gd and Tm. Moreover, separate alloy phases of Si, Fe, Ti, and ITEs that can be easily separated were obtained. Among these alloy phases, Ti and Fe are found to be enriched in the Si–Fe and Si–Fe–Ti alloy phases, and the total content of REEs, Th and U in the ITEs phase accounts for 82.61 wt%. This product can be easily broken and separated and has the application potential for purification in a vacuum environment. The process is simple and environmentally friendly and does not require too many auxiliary materials. Moreover, it can be used for the direct collection and enrichment of rare and precious elements with lower grades. This study realizes a simple process extraction route suitable for a variety of lunar mare resources and provides a reference for ISRU and the extraction of low-grade scarce resources.

Acknowledgment

The authors would like to thank Kairui Tai and Sizhe Zhao for their assistance with the experiments and for providing high-grade monazite samples.

References

1. Che XC, Nemchin A, Liu DY, Long T, Wang C, Norman MD, et al. Age and composition of young basalts on the Moon, measured from samples returned by Chang'e-5. *Science*. 2021;374(6569):887.
2. Crawford IA. Lunar resources: a review. *Prog Phys Geogr*. 2015;39(2):137.
3. Benaroya H. Lunar habitats: a brief overview of issues and concepts. *REACH Rev. Hum. Space Explor*. 2017;7:14.
4. Heiken GH, Vaniman DT, French BM. *Lunar Sourcebook, a user's guide to the Moon*1. Cupertino: Archive; 1991.
5. Johnson T, Morrissey L, Nemchin A, Gardiner N, Snape J. The phases of the Moon: modelling crystallisation of the lunar magma ocean through equilibrium thermodynamics. *Earth Planet Sci Lett*. 2021;556, 116721.
6. Anand M, Crawford IA, Balat-Pichelin M, Abanades S, Van Westrenen W, Péraudeau G, et al. A brief review of chemical and mineralogical resources on the Moon and likely initial in situ resource utilization (ISRU) applications. *Planet. Space Sci*. 2012;74(1):42.
7. Abreu N, Aponte J, Cloutis E, Nguyen A. The Renazzo-like carbonaceous chondrites as resources to understand the origin, evolution, and exploration of the solar system. *Geochemistry*. 2020, 125631.
8. Altun AA, Ertl F, Marechal M, Makaya A, Sgambati A, Schwentenwein M. Additive manufacturing of lunar regolith structures. *Open Ceram*. 2021;5, 100058.
9. Chen ZH. Global rare earth resources and scenarios of future rare earth industry. *J Rare Earths*. 2011;29(1):1.
10. McLeod CL, Krekeler M. Sources of extraterrestrial rare earth elements: to the moon and beyond. *Resources*. 2017;6(3):40.
11. Caprio L, Demir AG, Previtali B, Colosimo BM. Determining the feasible conditions for processing lunar regolith simulant via laser powder bed fusion. *Addit Manuf*. 2020;32, 101029.
12. Isachenkov M, Chugunov S, Akhatov I, Shishkovsky I. Regolith-based additive manufacturing for sustainable development of lunar infrastructure–An overview. *Acta Astronaut*. 2021;180:650.
13. Iwata TJAA. Technical strategies for lunar manufacturing. *Acta Astronaut*. 1992;26(1):29.
14. Kim HG, Kim WR, Kwon O, Bang GB, Ham MJ, Park H-K, et al. Laser beam melting process based on complete-melting energy density for commercially pure titanium. *J Manuf Process*. 2019;45:455.
15. Lin T-C, Cao C, Sokoluk M, Jiang L, Wang X, Schoenung JM, et al. Aluminum with dispersed nanoparticles by laser additive manufacturing. *Nat Commun*. 2019;10(1):1.
16. Nieke P, Kita J, Häming M, Moos R. Manufacturing dense thick films of lunar regolith simulant EAC-1 at room temperature. *Materials*. 2019;12(3):487.
17. Lomax BA, Conti M, Khan N, Bennett NS, Ganin AY, Symes MD. Proving the viability of an electrochemical process for the simultaneous extraction of oxygen and production of metal alloys from lunar regolith. *Planet Space Sci*. 2020;180, 104748.
18. Schlüter L, Cowley A. Review of techniques for *In-Situ* oxygen extraction on the moon. *Planet Space Sci*. 2020;181, 104753.
19. Schwandt C, Hamilton JA, Fray DJ, Crawford IA. The production of oxygen and metal from lunar regolith. *Planet Space Sci*. 2012;74(1):49.
20. Hui HJ, Guan YB, Chen Y, Peslier AH, Zhang YX, Liu Y, et al. A heterogeneous lunar interior for hydrogen isotopes as revealed by the lunar highlands samples. *Earth Planet Sci Lett*. 2017;473:14.
21. Lv W, Lv XW, Xiang JY, Hu K, Zhao SQ, Dang J, et al. Effect of preoxidation on the reduction of ilmenite concentrate powder by hydrogen. *Int J Hydrogen Energy*. 2019;44(8):4031.
22. Sargeant H, Abernethy F, Anand M, Barber S, Landsberg P, Sheridan S, et al. Feasibility studies for hydrogen reduction of ilmenite in a static system for use as an ISRU demonstration on the lunar surface. *Planet Space Sci*. 2020;180, 104759.
23. Ihsanullah. Carbon nanotube membranes for water purification: developments, challenges, and prospects for the future. *Separ Purif Technol*. 2019;209:307.
24. Liu Y, Guan Y, Zhang Y, Rossman GR, Eiler JM, Taylor LA. Direct measurement of hydroxyl in the lunar regolith and the origin of lunar surface water. *Nat Geosci*. 2012;5(11):779.
25. Newcombe ME, Brett A, Beckett JR, Baker MB, Newman S, Guan Y, et al. Solubility of water in lunar basalt at low pH_2O. *Geochem Cosmochim Acta*. 2017;200:330.
26. Peslier AH. A review of water contents of nominally anhydrous natural minerals in the mantles of Earth, Mars and the Moon. *J Volcanol Geoth Res*. 2010;197(1–4):239.
27. Just G, Smith K, Joy K, Roy M. Parametric review of existing regolith excavation techniques for lunar in Situ Resource Utilisation (ISRU) and recommendations for future excavation experiments. *Planet Space Sci*. 2020;180, 104746.
28. Naser M. Extraterrestrial construction materials. *Prog Mater Sci*. 2019;105, 100577.
29. Dang J, Zhang GH, Chou KC. Kinetics and mechanism of hydrogen reduction of ilmenite powders. *J Alloys Compd*. 2015;619:443.
30. Chen GZ, Fray DJ, Farthing TW. Direct electrochemical reduction of titanium dioxide to titanium in molten calcium chloride. *Nature*. 2000;407(6802):361.
31. Arinicheva Y, Popa K, Scheinost AC, Rossberg A, Dieste-Blanco O, Raison P, et al. Structural investigations of (La,Pu)PO_4 monazite solid solutions: XRD and XAFS study. *J Nucl Mater*. 2017;493:404.
32. Janots E, Brunet F, Goffé B, Poinssot C, Burchard M, Cemič L. Thermochemistry of monazite-(La) and dissakisite-(La): implications for monazite and allanite stability in metapelites. *Contrib Mineral Petrol*. 2007;154(1):1.
33. Neumeier S, Kegler P, Arinicheva Y, Shelyug A, Kowalski PM, Schreinemachers C, et al. Thermochemistry of $La_{1-x}Ln_xPO_4$-monazites (Ln= Gd, Eu). *J Chem Thermodyn*. 2017;105:396.
34. Sun JL, Liu CJ, Jiang MF. Phosphorus fixation capacity of CaO-SiO_2-Al_2O_3-MnO-Ce_2O_3 slag based on structural considerations. *J Rare Earths*. 2023;41(3):446.
35. Quan ZH, Wang ZF, Wang XT, Liu H, Ma Y. Effects of Sm_2O_3 addition on sintering behavior of pre-synthesized magnesia-rich magnesium aluminate spinel. *J Rare Earths*. 2021;39(11):1450.
36. Liu QS, Tu T, Guo H, Cheng HJ, Wang XZ. High-efficiency simultaneous extraction of rare earth elements and iron from NdFeB waste by oxalic acid leaching. *J Rare Earths*. 2021;39(3):323.
37. Bale CW, Chartrand P, Degterov S, Eriksson G, Hack K, Mahfoud RB, et al. FactSage thermochemical software and databases. *Calphad*. 2002;26(2):189.
38. Bale CW, Bélisle E, Chartrand P, Decterov S, Eriksson G, Gheribi A, et al. Reprint of: FactSage thermochemical software and databases, 2010–2016. *Calphad*. 2016;55:1.
39. Hasegawa M. *Ellingham diagram*. Amsterdam: Elsevier; 2014:507.
40. Hosseinpour A, Tafaghodi Khajavi L. Slag refining of silicon and silicon alloys: a review. *Miner Process Extr Metall Rev*. 2018;39(5):308.
41. Yang SC, Wan XH, Wei KX, Ma WH, Wang Z. Silicon recovery from diamond wire saw silicon powder waste with hydrochloric acid pretreatment: an investigation of Al dissolution behavior. *Waste Manage (Tucson, Ariz)*. 2021;120:820.
42. Yang SC, Wan XH, Wei KX, Ma WH, Wang Z. Silicon recycling and iron, nickel removal from diamond wire saw silicon powder waste: synergistic chlorination with CaO smelting treatment. *Miner Eng*. 2021;169, 106966.